Research Article | Vol. 28, No. 17 / 17 August 2020 / Optics Express 24874
Optics EXPRESS

Ultrafast electro-optical disk modulators for logic, communications, optical repeaters, and wavelength converters

DUSAN GOSTIMIROVIC,[1,*] FRANCESCO DE LEONARDIS,[2] RICHARD SOREF,[3] VITTORIO M. N. PASSARO,[2] AND WINNIE N. YE[1]

[1]Department of Electronics, Carleton University, 1125 Colonel By Drive, Ottawa, ON K1S 5B6, Canada
[2]Department of Electrical and Information Engineering, Politecnico di Bari, via E. Orabona n. 4, 70125 Bari, Italy
[3]Engineering Department, University of Massachusetts at Boston, 100 Morrissey Boulevard, Boston, Massachusetts 02125, USA
*dusan.gostimirovic@carleton.ca

Abstract: We propose a U-shaped pn junction in a silicon-on-insulator microdisk resonator to effectively double the junction–mode overlap in the state-of-the-art, vertical pn junction microdisk electro-optical (EO) modulators. The U-shaped pn junction promotes the maximum overlap between the junction depletion zone and the whispering gallery optical mode in the microdisk. By fully depleting the p region of the npn-sequenced U-junction, the capacitance is reduced below 3 fF, which significantly improves the speed and power performance. In this work, we implement the high-efficiency, depleted U-junction design to maximize the operating bandwidth of EO modulators, EO logic elements, EO 2×2 switches for wavelength-division cross-connects, 2×2 reconfigurable optical add–drop multiplexers, optical-to-electrical-to-optical (OEO) repeaters-with-gain, OEO wavelength converters, and 2×2 optical–optical logic gates. These devices all operate in the 7.6-to-50 GHz bandwidth range with ultralow energy consumption between 0.4 and 9.8 fJ/bit. By using CMOS-compatible materials and fabrication-feasible design dimensions, our proposed high-performance devices offer a promising potential in next-generation, high-volume electro-optical communications and computing circuits.

1. Introduction

This theoretical, simulation-based study proposes a high-efficiency bus-coupled electro-optical microdisk modulator design for ultrahigh-speed and low-power communications and computing applications on the silicon-photonics integrated-chip platform. The proposed modulator features a depletion-mode U-shaped pn junction which maximizes the depleted junction overlap with the whispering gallery mode (WGM) of the microdisk. Consequently, a maximum change in the disk's effective refractive index can be induced, thereby leading to a large resonance wavelength shift per volt applied to the junction. The high modulation efficiency achieved by this design allows for a low-Q resonant operation at suitably low voltages to circumvent the speed–power trade-off in conventional resonator-based modulator designs [1–7] while maintaining an ultracompact footprint and high extinction ratio (ER).

We design our modulator on the silicon-on-insulator (SOI) platform [8,9] to enable low-cost and high-volume production of CMOS-compatible photonic and electro-optical (EO) circuits. We optimize the proposed modulator for use in optical communications, switching, and computing applications. The first device investigated is a stand-alone electro-optical modulator (EOM). A pulley-style coupler [10–12], in which the bus waveguide bends around the disk, is used to tailor the waveguide–disk coupling condition for a high ER with low Q factors required for operating at high speeds. A second bus waveguide, also in the pulley coupler configuration, is added in

#400716 https://doi.org/10.1364/OE.400716
Journal © 2020 Received 22 Jun 2020; revised 22 Jul 2020; accepted 25 Jul 2020; published 7 Aug 2020

Optics EXPRESS

the second modulator device. This 2×2 device can be utilized in important communications and computing applications, such as electro-optical logic (EOL) gates [11,13–15], wavelength-division multiplexed (WDM) NxNxMλ spatial routing switches [16,17], and reconfigurable optical add-drop multiplexers (ROADMs) [18,19]. For the two-bus configuration, the coupling angle of both pulleys is adjusted to maintain high ER and low Q factor values.

We also demonstrate the implementation of the proposed modulator in multifunctional optical-to-electrical-to-optical (OEO) devices for optical signal restoration-with-gain, wavelength conversion, and optical–optical logic (OOL). In these OEO devices, a CMOS-compatible, GeSn 1,550-nm photodetector (PD) is used to convert a premodulated optical input signal into a photocurrent, which drives the DC-biased circuitry of the EOM [11]. The EOM, in turn, modulates a separate, continuous wave (CW) optical signal injected from the disk's input bus. By using a similar or higher intensity for the CW signal, this process effectively restores the intensity of the original signal that is incident upon the PD, thus adding optical gain to that signal. The OEO device, in addition to working as an "amplifier-less" optical repeater, can work as a wavelength converter by using a different wavelength for the CW signal. The second application of the OEO configuration adds a second PD-driven electrical input and a second bus waveguide to the EOM to perform a full set of OOL operations. With the two (waveguide-PD) inputs required of a logic gate, this device simultaneously performs OR, AND, and XOR operations, as well as their inversions: NOR, NAND, and XNOR, employing only a single microresonator.

Given the high modulation efficiency of the depletion-mode U-junction modulator, the EOM, EOL, NxNxMλ cross-connect, ROADM, OEO repeater/converter, and OOL all operate, as optimized in this paper, between 7.6 and 50 GHz in bandwidth, with suitably low levels of energy consumption, between 0.4 and 9.8 fJ/bit, while maintaining more than 10 dB ER in an ultracompact, 2-μm-radius disk.

This paper presents the design and optimization of the U-junction microdisk modulator and its implementation in several real and proposed applications in computing and communications. Primary design considerations are made to maximize operating bandwidth using CMOS-compatible features and materials. Although an experimental demonstration of the devices is not included here, special considerations on their fabrication feasibility are discussed and are supplemented with numerical analysis. This work presents a feasible design approach to enhance the performance of electro-optical devices in next-generation communications and computing circuits.

2. High-bandwidth resonant 1×1 and 2×2 EO devices

Figures 1 and 2 present the four devices optimized in this paper for ultrahigh bandwidth. The real and potential applications of the devices are as follows. The modulator shown in Fig. 1(a) could form the heart of a chip-scale data transmitter that feeds an optical fiber, or it could function as an EO logic element where many such 1×1s are deployed to create a complex on-chip logic photonic integrated circuit (PIC); while for the Fig. 1(b) 2×2, the EO logic gates shall have complimentary outputs. The 2×2 switch in Fig. 1(b) (often used as 1×2 in high-radix matrix switches [20]) also has some major applications in NxNxMλ cross-connect switches [21]. Interesting microring-based WDM cross-connect architectures have been proposed recently for waveguide-connected sets of the Fig. 1(b) devices [16,22,23]. The performance predicted here for our Fig. 1(b) disks suggests that they are a better choice than EO microring resonators for the data-center matrix switching application. In Fig. 2, each diode symbol represents a strip waveguide with its own waveguide PD at the strip end, while its output provides the electrical drive (which is demodulated from the original optical signal) for the new higher-intensity CW signal entering the disk. A required load resistor R_L is placed in shunt with the EOM input terminals because this resistance value is chosen to convert the PD photocurrent into the required reverse-bias voltage on the disk. The primary use of the structures in Fig. 2 is the "amplifier-less"

Optics EXPRESS

optical repeater; that is, a device that restores or increases the amplitude of light incident on the PD by transferring its data to a new higher-intensity CW signal. This OEO is equivalent in many ways to a semiconductor optical amplifier. The motivation for the OEOs is to deploy a group of such "gain" elements within a "large-scale" photonic integrated circuit to restore signals that become attenuated when traveling through the circuit. As a wavelength converter, this OEO design is attractive because it can change the operating wavelength while adding gain. The OOL application, while fascinating in principle, needs specialized computer architectures to fully exploit its potential in advancing the electronic–photonic digital computer.

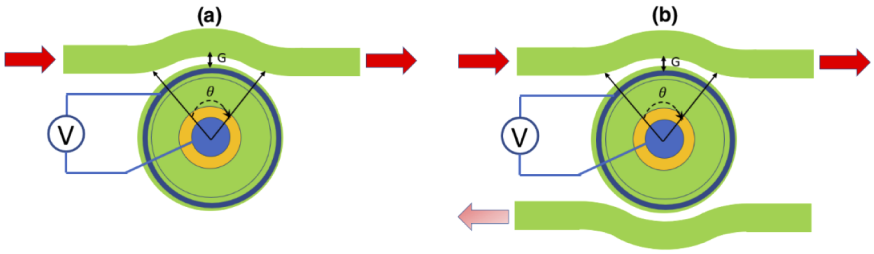

Fig. 1. Top view of the EO microdisk standing alone for (a) EOM and (b) EO 2 × 2 "switch" for EO logic, WDM cross-connect switching networks, and ROADMs. Metal contact regions are shown in blue. The coupling angle and gap size between the disk and the bus waveguide are denoted by θ and *G*, respectively.

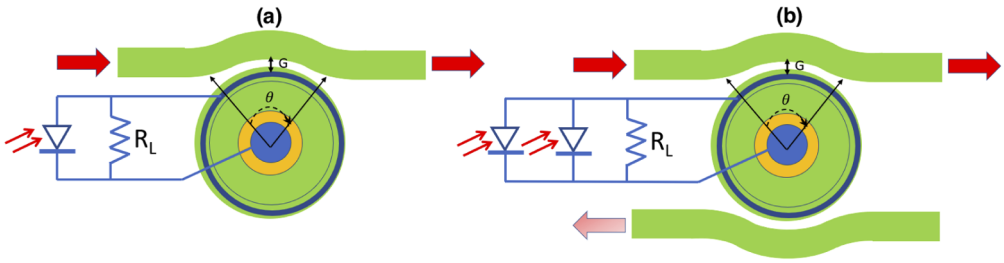

Fig. 2. Top view of the photodetector-driven EO microdisk for OEO repeaters-with-gain and for OEO wavelength converters, and (b) the 2 × 2 device for multi-operational optical–optical logic gates. Each diode symbol represents a separate strip waveguide with its own waveguide PD at the strip end (two such waveguides for the OOL), as in Ref. [11].

The high bandwidth targeted in this paper for the device structures illustrated in Figs. 1 and 2 serves three purposes: it provides an extremely high (i) "information bandwidth" for analog or digital modulation of light in an optical interconnect or communications link, (ii) bit/sec rate for digital modulation—a rate that is about twice the optical bandwidth, and (iii) switching rate, or rate of "reconfiguration" for 2 × 2 switching elements.

3. Designing a high-bandwidth microdisk modulator

We begin our simulations with an investigation of the device in Fig. 1—a stand-alone EOM. Here, our U-junction depletion-mode microdisk modulator is a silicon rib-edge disk that is side coupled to one or two silicon strip bus waveguides. The rib-to-strip-bus side coupling is similar to that of a fully etched disk.

The design considerations of this device are made to maximize bandwidth for optical communications and computing applications. The standard, 220-nm-thick silicon core with a buried 3-μm silicon dioxide platform is used with an ultracompact disk radius of 2 μm to

Optics EXPRESS

minimize the overall device footprint. The key feature of our microdisk modulator is the U-shaped pn junction, as shown in Fig. 3, which is designed to maximize its depletion overlap with the WGM of the disk cavity. Vertically oriented pn junctions naturally overlap better with the wide aspect ratio of the SOI modes [24–27]; the U-shaped junction is effectively a double vertical pn junction, with an n-p-n vertical sequence. A 50-nm-thick outer slab region (rib platform) is used to host the circular cathode contact to the U-shaped n region. The rib-shaped perimeter delivers good coupling to the bus waveguides—a coupling similar to that of fully etched disks. Previous demonstrations of microdisk modulators kept both electrodes within the WGM [24,25], but this creates highly doped pn junctions that add to the total device capacitance (energy consumption) without contributing to the free-carrier plasma effect. Our design only has two pn junctions: (i) the main, U-shaped junction that contributes to modulation and (ii) the small parasitic junction between the p+ region and the top of the n region. The depth of the p+ region is kept shorter than the depth of the silicon so as not to make a junction with the bottom n region. This is a unique structure with rather complex fabrication requirements; however, a U-junction of similar feature sizes has been successfully demonstrated in other fabricated SOI devices [26].

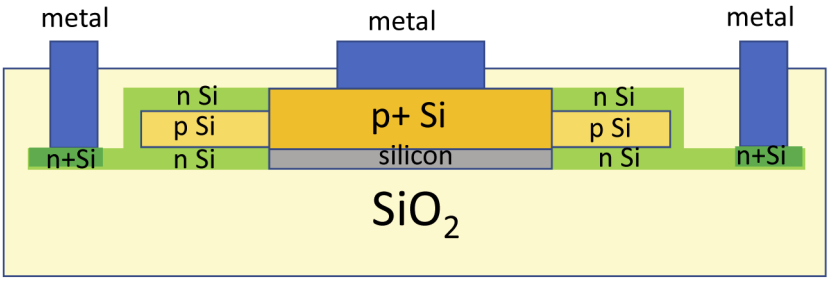

Fig. 3. Cross-section view of the U-junction depletion-mode microdisk modulator.

The microdisk resonator has several advantages over the microring resonator. The disk configuration is more efficient for hosting vertical pn junctions [15,24,25]. Furthermore, as detailed in Ref. [24], the plot of the internal quality factor as a function of radius for microdisk and microring resonators shows better performances for the microdisks as a result of the higher optical confinement. Moreover, the TE radial mode profiles indicate larger bending losses for microring resonators with radii around 2 μm. Our disk is different from that in Ref. [24] as it has an outer rib platform; however, without the etched inner wall of a microring, the WGM of the disk still expects to experience less loss through less sidewall roughness. This is very important for highly compact devices such as ours. Furthermore, disks offer higher resistance to thermal and fabrication variations [28]. The higher resistance to thermal variations means less static energy consumption is required to keep the disk set to the desired wavelength.

The free-carrier plasma dispersion effect triggers the free carriers of the doped silicon regions to induce a change in the real and imaginary refractive indices of the silicon. By reverse biasing a pn junction, the depletion width is increased, and the spatial change in the free-carrier concentration produces a small but effective change in the refractive index. The concentration, orientation, and boundaries of the doped silicon regions are optimized to achieve the maximum change in effective refractive index Δn_{eff} of the WGM, while keeping the carrier-induced loss low. The boundaries of the highly doped, n+ and p+ regions are placed just far enough away from the WGM to minimize contact resistance without adding significant carrier-induced loss. The p region is placed in the vertical center of the disk because holes produce a greater change in refractive index than electrons, as indicated by the Soref–Bennett equations [29]. The commercial drift–diffusion solver from Lumerical (CHARGE) [30] is used to calculate the charge profiles of the device for different reverse biases and doping parameters. These are exported to the mode

Optics EXPRESS

solver from Lumerical (MODE) [30] to calculate the effective refractive index and loss of the WGM for each bias condition.

For high-bandwidth operation, a microresonator-based modulator must operate with a low Q factor in order to minimize the photon lifetime delay within its cavity. Low-Q modulators, which have "wide" resonance transmission peaks, have in the past required increased reverse biases to maximize the modulation depths with inevitably high energy consumption. With the high $\Delta n_{eff}/V$ achieved by the present design, high-speed, low-Q resonators can be modulated at reasonably low reverse biases.

A parameter sweep of the peak doping concentration N and implant depth (range) R_p is performed to optimize the bandwidth within a reasonable voltage range of 0 to -4 V and with a realistic p-region straggle of $\Delta R_p = 40$ nm (as determined by the TCAD simulations in Sec. 4). This device achieves its peak bandwidth with $N = N_A = N_D = 1.5 \times 10^{18}$ cm^{-3} and $R_p = 110$ nm, for a high Δn_{eff} of 3.5×10^{-4} V^{-1} (at a -1 V bias). The critical performance metrics of the optimized U-junction microdisk modulator are plotted in Fig. 4. Figure 4(a) plots the device capacitance as a function of reverse bias, which effectively demonstrates the behaviour of the U-junction. As the reverse bias is increased, the width of the depletion region is increased, which steadily decreases the capacitance. As the reverse bias is increased past -3.25 V, the capacitance drops off significantly. At this bias, the narrow middle p region becomes almost fully depleted, and the n-p-n vertical sequence effectively becomes an n-i-n. Operating in the fully depleted region, at -3.75 V, is beneficial for high-speed and low-power operation, as the U-junction capacitance C_{pn} is only 2.4 fF, and the total device capacitance C_{total} is 2.8 fF. Figure 4(b) uses the device capacitance and reverse voltage values to calculate $E/bit = CV^2/4$. This plot starts to follow the quadratic nature of the equation; however, it also drops off once the p region becomes depleted and capacitance is minimized. At the minimum capacitance point at -3.75 V, $E/bit = 9.8$ fJ/bit. The device can be operated in the low-bias region, for less than 5 fJ/bit of operation, but the minimum Q factor and maximum modulation speed are affected. Figure 4(c) presents the wavelength shift per volt produced at a given bias. The calculated wavelength shift is used to determine the minimum Q factor to design for, as any lower Q (i.e., with a wider resonance width) cannot be fully shifted by the given bias point. At the operating bias of -3.75 V, the device shifts 640 pm (170 pm/V), with an ultralow minimum Q of 2,427. It is clear from these plots that operating in the fully depleted region permits simultaneous high speed and low power performance. It should be noted that, although the device performs better at high reverse biases, the efficiency drops off significantly past the full depletion point, as there is no more pn junction to modulate. The full depletion of the p region is demonstrated in Fig. 5, which shows the free-carrier profile of the junction for 0 and -3.5 V biases.

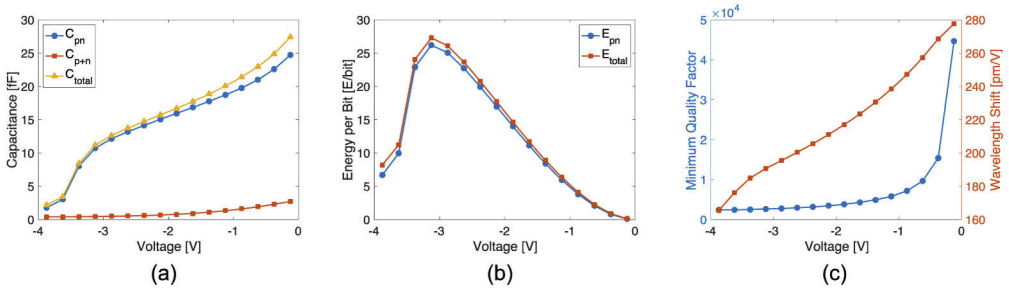

Fig. 4. (a) Capacitance, (b) energy consumption (in fJ/bit), and (c) resonance wavelength shift and minimum operating Q factor, with respect to reverse bias, for the stand-alone U-junction microdisk EOM devices presented in Fig. 1.

Optics EXPRESS

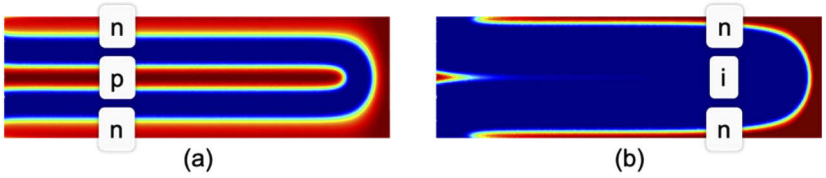

Fig. 5. Free-carrier profiles of the U-junction for (a) 0 and (b) -3.5 V biases. For -3.5 V, the p region is almost fully depleted; however, a small concentration of holes still exists at the interface with the p+ region (not shown). The depletion region is shown in blue, and the free carriers (both p and n) are shown in red.

We now present the bandwidth analysis of our devices. The EOM in Fig. 1(a) couples a single bus waveguide to the microdisk, where a reverse bias is applied to the U-junction. A pulley-style coupler is used in all four of the proposed devices because the coupling condition (and the disk's Q factor) can be adjusted by simply changing the coupling angle (θ) around the disk. By increasing the degree of bending around the disk, we lower the Q factor and photon lifetime of the resonator and increase the potential bandwidth. Figure 6 plots the maximum bandwidth of the device with respect to the applied reverse bias. The maximum bandwidth of the device is a function of the photon (optical) and RC (electrical) lifetimes of the microdisk and pn junction, respectively, which can be estimated by [11]

$$\Delta f_{3dB,opt} = \sqrt{\sqrt{2}-1}\frac{c_0 \delta\lambda}{\lambda_0^2} \tag{1}$$

$$\Delta f_{3dB,elec} = \frac{1}{2\pi RC} \tag{2}$$

$$\Delta f_{3dB,total} = \frac{\Delta f_{3dB,elec}\Delta f_{3dB,opt}}{\sqrt{(\Delta f_{3dB,elec})^2 + (\Delta f_{3dB,opt})^2}}, \tag{3}$$

where c_0 is the vacuum speed of light, λ_0 is the resonance wavelength, $\delta\lambda$ is the linewidth of the resonance, and R and C are the resistance and capacitance of the U-junction, respectively.

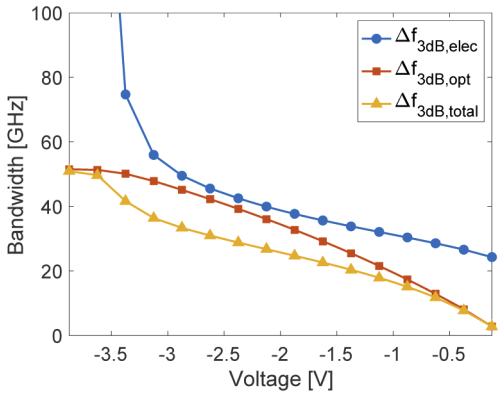

Fig. 6. Optical, electrical, and total bandwidth, with respect to reverse bias, for the stand-alone U-junction microdisk EOM devices presented in Fig. 1.

As the reverse bias increases, the pn junction induces a greater $\Delta\lambda$ in the resonance of the microdisk resonator, which enables the use of high-$\delta\lambda$, low-Q disks. At the same time, the

Optics EXPRESS

depletion width expands, and the edges of the n region move slowly away from the center of the WGM, where the carrier dispersion effect peaks. We see this effect through the slow saturation of the optical bandwidth until -3.75 V, where the middle p region is fully depleted, and the bandwidth curve flattens out completely. By increasing the straggle of the p region in the U-junction, the full bandwidth flattening would occur at a larger reverse bias, but the peak bandwidth would be lower, limited by the modulation efficiency with less junction–mode interaction.

Electrical bandwidth is a product of the pn junction capacitance and contact resistance in the electrodes. The resistance was calculated to be 265 Ω using the drift–diffusion solver from Lumerical. As the reverse bias is increased past the full junction depletion, capacitance is significantly reduced and the electrical bandwidth significantly increases; thus, the total bandwidth is entirely limited by optical bandwidth, as illustrated in Fig. 6. At -3.75 V, the EOM operates at 50.3 GHz and 9.8 fJ/bit.

The carrier-induced loss of the EOM is 27.6 and 10.8 dB/cm for 0 and -3.75 V, respectively. Because a maximum bandwidth is achieved at an ultralow Q factor of 2,427, this loss does not significantly affect the ultimate operation of the device. However, the pulley-coupled waveguide must still be optimized to achieve the desired Q factor with a maximum ER. Our preliminary investigations, as shown in Fig. 7(a), indicate that the required Q induces an ER value of only ~3 dB. Note that in our optical calculations, we are taking the simulated carrier-induced loss and the standard, 2 dB/cm waveguide propagation loss into account. We consider the bending loss to be negligible compared to these two. Because ER and Q both decrease with an increase in coupling angle, there is a trade-off between ER and bandwidth for this 1×1 EOM. This trade-off does not exist for low coupling angles, as ER increases with a reduced Q, but the Q values are too high for high-speed operation. To ensure high-performance operation, we shall impose a requirement on all devices presented in this work: that they must offer an ER of at least 10 dB. To satisfy this condition, the first device must operate with a minimum Q of 8,382, which is achieved with a coupling angle of $\theta = 18.5°$, a gap size of $G = 100$ nm (as with each device presented here), and a waveguide width of 500 nm. At this Q, the bandwidth, bias, and energy consumption are all reduced to 13.4 GHz, -0.75 V, and 3.1 fJ/bit, respectively. Should a lower ER be acceptable, the coupling angle and applied bias can simply be increased to the desired higher bandwidth. The previous discussion is summarized in Fig. 7(a), where both the Q and the ER values are plotted as a function of the coupling angle, assuming $N_A = N_D = 1.5 \times 10^{18}$ cm^{-3}, a bus waveguide width of 500 nm, and a reverse voltage of -0.75 V. Under the same conditions, the transmission spectrum as a function of the wavelength shift, $\Delta\lambda = \lambda - \lambda_0$, is shown in Fig. 7(b), for different values of the reverse bias and assuming a fixed coupling angle of 18.5°. The applied bias affects the critical coupling condition to the microdisks, reflecting the changes in the ER of the resonances.

3.1. Two-bus ROADM and EO matrix element switch

The 2×2 switch in Fig. 1(b) adds a second pulley bus waveguide to the EOM for high-speed switching in WDM communications. Figures 4–6 hold true for this device, as the pn modulator itself remains the same. The addition of the second bus waveguide, however, changes the coupling condition, as the WGM now has two output accesses. Figures 8(a) and 8(b) show the Q factor and the ER at the Through port, as a function of the coupling angle, for different values of the bus waveguide width W_{bus}, and assuming a reverse voltage of -3.75 and -1.25 V, respectively. The plots clearly indicate that for the greater coupling angle required for a low-Q operation, the ER now increases, which removes the trade-off with bandwidth; hence, the device can operate at its maximum bandwidth without dropping below the 10 dB ER target. With a waveguide width of 500 nm, and a coupling angle of 29.6°, the 2-bus ROADM and EOL element achieves the maximum, 50.3 GHz bandwidth with an ER of 24.4 dB. Operating in the low-bias region (e.g., -1.25 V) requires a larger Q factor of 5,310, which limits ER and bandwidth to 12.4 dB and 19.1 GHz, respectively, but with a reduced *E/bit* of 7.6 fJ/bit. For low-bias operation, the coupling

Optics EXPRESS

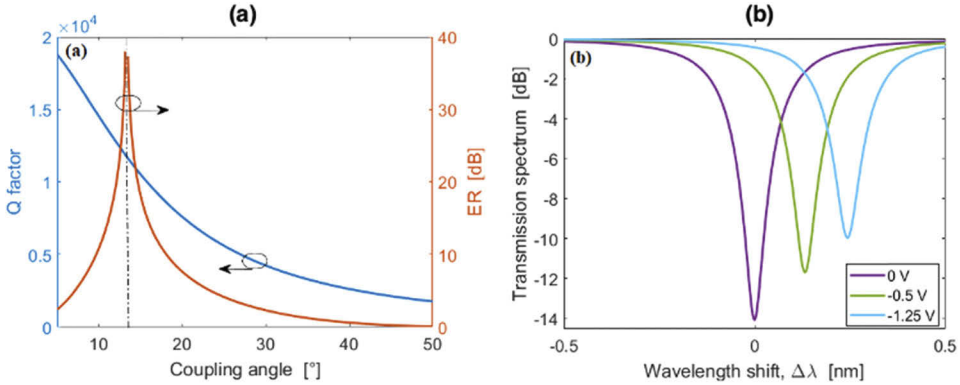

Fig. 7. (a) Q factor and ER at the Through port, as a function of the coupling angle, assuming a reverse voltage of -0.75 V; (b) Through-port transmission spectrum as a function of the resonance wavelength shift, for different values of the reverse bias. In the simulations we have assumed a waveguide width of 500 nm, $N_A = 1.5 \times 10^{18}$ cm^{-3}, $N_D = 1.5 \times 10^{18}$ cm^{-3}, and a coupling angle of 18.5°.

angle and waveguide width were adjusted to 28.0° and 600 nm, respectively, to maximize ER and bandwidth.

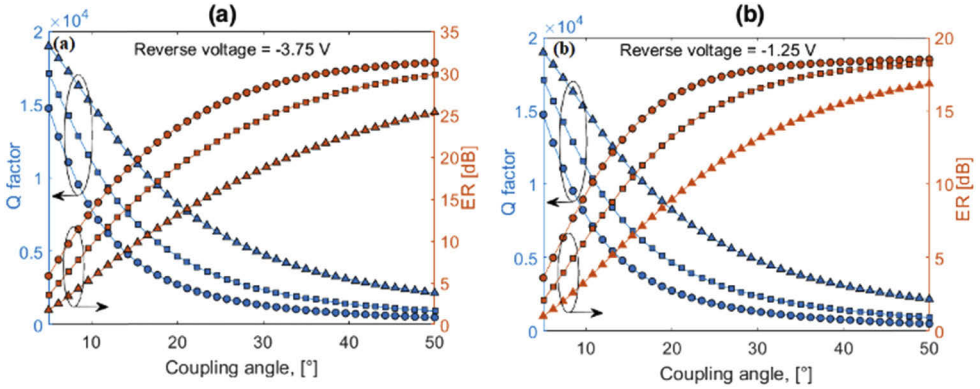

Fig. 8. Q factor and ER at the Through port, as a function of the coupling angle, for different values of the bus waveguide width. In (a), the reverse bias is -3.75 V; and in (b), the reverse bias is -1.25 V. Circle: $W_{bus} = 400$ nm, Square: $W_{bus} = 500$ nm, Triangle: $W_{bus} = 600$ nm. The peak carrier concentrations of the doping regions are $N_A = N_D = 1.5 \times 10^{18}$ cm^{-3}.

3.2. *Optical–electrical–optical repeater and wavelength converter*

The OEO repeater and wavelength converter presented in Fig. 2(a) follows the same design as the EOM in Fig. 1(a), but with an added load resistor R_L connected across the pn junction, which is driven by the PDs photovoltage V_{ph}. V_{ph} is a function $\eta_{pd} P_{in} R_L$, where η_{pd} is the responsivity of the PD in photoconductive mode and P_{in} is the peak power of the PD's inputted optical signal. From Ref. [11], we estimate the responsivity of the GeSn PD to be 1.4 A/W, using a suitable optical input power of 0.5 mW. In our device architectures, the p-i-n PD is a p-GeSn/i-GeSn/n-GeSn homo-junction photodiode embedded in a ridge waveguide. In particular, the GeSn waveguide is a ridge structure with a height of H_{PD}, a width of W_{PD}, and a slab thickness of H_s. The ion implantation is performed at both lateral ends of the slab in order

Optics EXPRESS

to fabricate the p and n regions, as well as the p++ and n++ contacts. Moreover, a Ge layer with a thickness d is necessary to facilitate the deposition of the GeSn alloy. As detailed in our previous work [11], the GeSn-on-Si PD presents a number of advantages compared to the standard Ge-on-Si PDs. In particular, (i) the GeSn-on-Si PD gives a better wavelength coverage due to its selectable bandgap; (ii) the 1,550-nm GeSn-on-Si PD has stronger absorbance (15,000 cm^{-1}), higher efficiency, and lower spatial volume; and (iii) hundreds or thousands of PDs could be closely integrated on-chip at a low cost. In the present work, we adopt 3% of Sn content in order to optimize its absorption at 1,550 nm.

As with the EOM in Fig. 1(a), because this device uses one bus waveguide, it must operate with a high Q to achieve a suitably high ER. The added load resistor also significantly limits its electrical bandwidth. We reduce the peak carrier concentration of the doping regions to $N_A = 0.8 \times 10^{18}$ cm^{-3} and $N_D = 1.5 \times 10^{18}$ cm^{-3} to deplete the p region at a lower reverse voltage and to reduce the required load resistance. To produce the -0.75 V photovoltage required for the maximum bandwidth operation, the required load resistance is 1.1 kΩ. Given a fully depleted, low-C junction, the electrical bandwidth is larger than the optical bandwidth; thus, the total bandwidth is effectively limited by the Q factor (ER). Figure 9 presents the bandwidth plots with the added load resistor, where the total bandwidth maxes out at 11.1 GHz. It is clear that the overall bandwidth performance is dominated by the optical bandwidth. With a coupling angle and waveguide width of 15° and 500 nm, respectively, this device achieves the required Q of 11,100 with an ER of 17.0 dB and an *E/bit* of 0.67 fJ/bit. The Through-port transmission spectrum of this device is shown in Fig. 10 for different reverse biases. Note that the smaller resonance shift between -0.5 and -0.875 V is due to the junction already being mostly depleted.

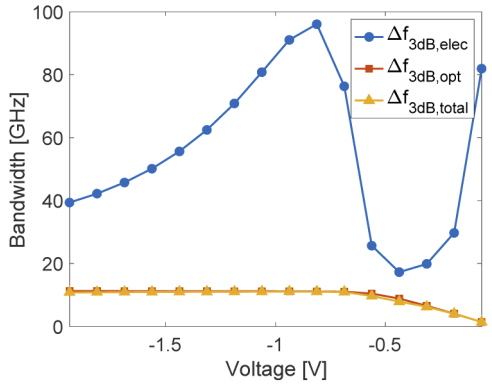

Fig. 9. Optical, electrical, and total bandwidth, with respect to the applied reverse bias, for the PD-driven U-junction microdisk OEO and OOL devices presented in Fig. 2. The sharp increase in electrical bandwidth is due to the sharp depletion of the middle p region; the decrease of electrical bandwidth past -1 V is due to R_L increasing with C already being at its minimum.

3.3. Optical–optical multi-operational logic gate

The restorative, multi-operational optical–optical logic gate follows the same connected PD–EOM design as the OEO (as shown in Fig. 2(b)); however, a second electrical input is added to perform 2-bit Boolean logic operations. The second electrical input is from an identical GeSn waveguide PD connected in parallel with the first PD. The total photovoltage is expressed by $V_{ph} = R_L I_1 + R_L I_2$, where I_1 and I_2 are the photocurrents generated by the two PDs. As demonstrated in Fig. 7 of our previous work [11], the two electrical inputs are used to perform the OR, AND, or XOR operations by shifting the resonance wavelength by Δλ (one input on) or 2Δλ (two inputs on),

Optics EXPRESS

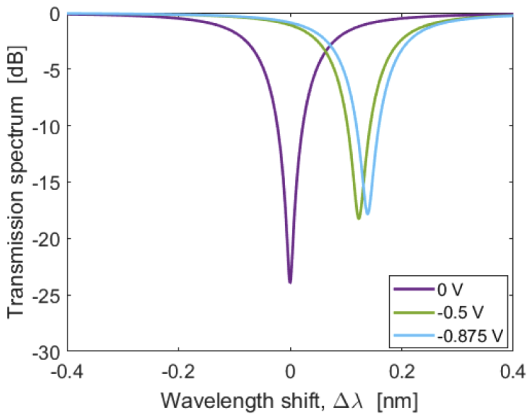

Fig. 10. Through-port transmission spectra of the OEO device in Fig. 2(a), as a function of the resonance wavelength shift, for different values of the reverse bias, assuming a waveguide width of 500 nm, a coupling angle of 15°, $N_A = 0.8 \times 10^{18}$ cm^{-3}, and $N_D = 1.5 \times 10^{18}$ cm^{-3}.

depending on the relative positions of the input and resonance wavelengths. With three input signals centered at λ_0, $\lambda_0 + \lambda$, and $\lambda_0 + 2\Delta\lambda$, this device performs the three fundamental logic operations simultaneously, for multiple instruction, single data (MISD) electro-optical computing. A second pulley coupler is added to the disk to capture the inverse of these operations as well, providing the complimentary NOR, NAND, and XNOR operations.

Adding the second bus waveguide to the OEO device configuration has the same effect the ROADM had, in that the ER increases with the coupling angle—eliminating the ER–bandwidth trade-off. Because of the negative impact the added load resistor has on the total bandwidth, the peak carrier concentration is reduced to $N = N_A = N_D = 0.8 \times 10^{18}$ cm^{-3} to increase bandwidth through a reduced capacitance. For this device, we cannot set V_{ph} to fully deplete the U-junction, as a second input would have no effect on modulation. We therefore set V_{ph} to half of the full depletion voltage. $1V_{ph}$ (one input on) is capable of shifting $1\Delta\lambda$ if we double the Q factor, and $2V_{ph}$ (two inputs on) will shift $2\Delta\lambda$. Because the U-junction is only partially depleted with $1V_{ph}$, the capacitance is higher, and we expect a slightly reduced maximum bandwidth compared to the OEO devices described in Sec. 3.2. With a coupling angle of 20°, a waveguide width of 600 nm, and a V_{ph} of -0.75 V, the OOL device achieves 7.6 GHz of operation, 2.2 fJ/bit of energy consumption, and an ER of 12.5 dB.

4. Fabrication feasibility

The ultimate implementation of the proposed junction design depends on the feasibility of its fabrication. Although the U-shaped design is uncommon, it has been experimentally demonstrated in other SOI devices with similar feature sizes [26]. These demonstrations indicate that the fabrication of a U-shaped junction is feasible. To further verify the feasibility of our optimized design, we carry out a TSUPREM-4 2D [31] process simulation.

The doped regions of the U-junction are created by ion implantation. We model our device using implant parameters within the capabilities of commercially available ion implantation services. The n region is created by two separate implants. The upper n region of the 1×1 and 2×2 EOM devices can be formed by implanting phosphorus with an energy and dosage of 20 keV and 3.8×10^{13} cm^{-2}, respectively, and the lower n region can be formed by implanting phosphorus with an energy and dosage of 120 keV and 0.7×10^{13} cm^{-2}, respectively. The middle p region of the U-junction can be formed by implanting boron with an energy and dosage of 20 keV and 3.8×10^{13} cm^{-2}, respectively. The doses can be increased or decreased to meet the

Optics EXPRESS

required concentrations of the other (OEO) devices, but the process remains the same. The p implant is the most demanding process step, as the straggle of the implant is low. After a thermal activation step of 1,000 °C for 5 s, the straggle of the p region ΔR_p is found to be 40 nm, which is used in the CHARGE optimizations. The n+ and p+ regions use a similar implant process, but with higher doses. The unbiased doping profile is shown in Fig. 11, where the peak concentrations and junction spacing closely match those of the CHARGE optimizations.

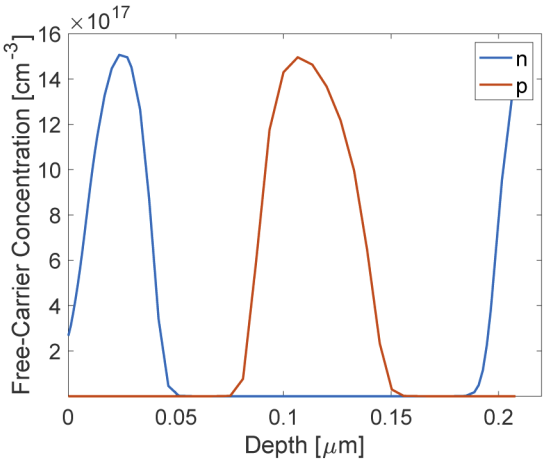

Fig. 11. TCAD-simulated vertical free-carrier concentration of the npn-sequenced U-junction modulator for a 0 V bias.

The passive component of our device: a disk with a 2 μm radius and a 100 nm waveguide-to-disk gap size, is readily fabricable by modern e-beam or deep UV lithography tools. The widths of the doping regions are no smaller than 2.4 μm (p+ region) and can be masked by the same lithography tools. The 50-nm spacing between the middle p region and the edge of the disk may cause a disconnection between the upper and lower n regions if there are significant mask misalignments. This gap can be widened to increase tolerance to misalignments; however, the junction–mode overlap (modulation efficiency) will consequently decrease.

To demonstrate the fabrication tolerance of our U-junction EOM design, we plot in Fig. 12, the bandwidth performance with respect to the range and straggle of the p region, the peak doping concentration, and the separation between the p region and the lateral edge of the disk (caused by variations in the size and lateral positioning of the p implant). With a 10% increase in the separation between the p region and the edge of the disk, the length of the pn junction is reduced, which reduces the modulation efficiency and maximum bandwidth by only 0.8%. For a 10% decrease in this separation, the length of the pn junction is increased, resulting in a 0.6% increase in the bandwidth. The efficiency will continue to increase (minimally) with the length of the pn junction until the separation is reduced to zero, where the two n regions become electrically isolated and the efficiency will be effectively halved. Extending or reducing the range of the p region by 10% causes one of the depletion zones to move further from the center of the WGM; hence, reducing the modulation efficiency. However, this only reduces the bandwidth by 2.6%, as the other depletion zone moves closer to the center of the WGM. By expanding or condensing the straggle of the p region by 10%, the U-junction will become fully depleted at a different reverse bias. Without adjusting the operating reverse bias, the bandwidth is reduced by as much as 16.1% for a larger p region straggle, and 13.1% for a smaller p region straggle. By adjusting the operating voltage to the new performance peak, the reduction is not as significant. Note that with a 15% increase in straggle, the outer n regions become very narrow; this reduces capacitance and increases electrical bandwidth. For 10% variations in peak doping concentration,

Optics EXPRESS

bandwidth reduces by as much as 12.3%, but this reduction can also be less significant if the operating reverse bias is adjusted to match where the U-junction is fully depleted. We believe that the fabricated devices will perform reasonably close to the optimal performance by providing appropriate tuning to the operating voltages.

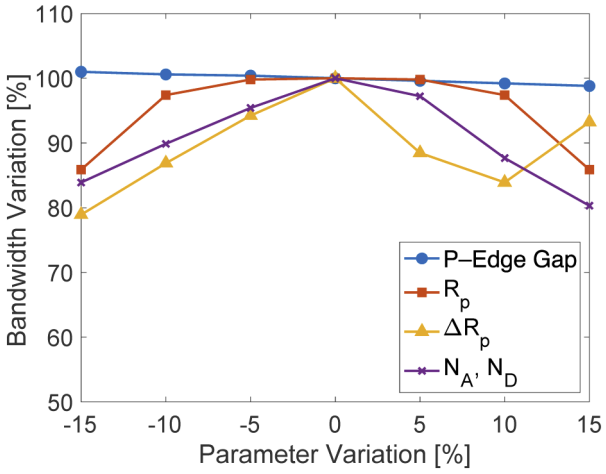

Fig. 12. Change in EOM bandwidth performance with respect to fabrication variations in separation between the p region and the lateral edge of the disk, range of the p implant R_p, straggle of the p implant ΔRp, and peak doping concentration N.

5. Summary of results

For all four of the devices depicted in Figs. 1 and 2, we summarize our simulation results in Table 1. The 2×2 EOM, because of its low device resistance and low-Q operation, achieves the largest bandwidth among the four devices, at 50.3 GHz. Although it uses a relatively large reverse bias of -3.75 V, the low device capacitance keeps the energy consumption low. The 2×2 OOL, which adds a large PD-driven load resistor to the 2×2 EOM, uses a lower peak doping to reduce the RC time delay through less capacitance. The lower doping concentration reduces its modulation efficiency, increases the minimum Q factor, and limits the total bandwidth. The 1×1 devices (stand-alone EOM and OEO repeater and wavelength converter) must operate at high Q factors to achieve suitably high ERs, which significantly limits their optical bandwidths. For high-Q operation, these devices naturally operate best at low voltages. We reduce the peak concentration of the doping regions to deplete the U-junction at these lower voltages. These devices operate at a relatively lower bandwidth with a low energy consumption. Each device is designed to achieve a minimum ER of 10 dB. Should a lower ER be acceptable, the Q factor can be reduced to increase the bandwidth.

Table 1. Summary of the Four Proposed U-Junction Modulator Devices

Device	Bandwidth (GHz)	Bias (V)	*E/bit* (fJ/bit)	Q Factor	ER (dB)	Coupling Angle (°)	W_{bus} (nm)
1×1 OEO	11.1	-0.875	0.7	11,100	17.0	15.0	500
2×2 OOL	7.60	-0.75	2.2	10,019	12.5	20.0	600
1×1 EOM	13.4	-0.75	3.1	8,382	10.0	18.5	500
2×2 EOM	50.3	-3.75	9.8	2,427	24.4	29.6	500
2×2 EOM (Low V)	19.1	-1.25	7.6	5,310	12.4	28.0	600

Optics EXPRESS

It should be highlighted that the 1×1 OEO has a reasonably high bandwidth with an ultralow energy consumption. The low drive voltage will enable arrays of these repeaters to be deployed in photonic integrated circuits at which the optical signal levels are in the low mW range. The 2×2 EOM is particularly promising for high-radix matrix optical network switching with impressive bandwidths at both voltage levels. The 1×1 EOM is expected to advance the art of EO logic with its excellent combination of performance metrics.

In comparison to our previous work on OEO and OOL devices [11], which featured a vertical pn junction design, we achieve a large energy efficiency improvement with a 2X bandwidth, while maintaining similar dimensions and ER performance, as shown in Tab. 2. A comparison to the state-of-the-art high-speed EOM devices is not straightforward, as our design direction—to reduce Q and increase bandwidth through high-efficiency pn junction designs—highlights the limitations of using 1×1 EOM configurations, where operating at low Q factors coincides with a low ER. In this work, we chose a minimum acceptable ER of 10 dB, which limits the bandwidth of our 1×1 EOM to 13 GHz. The state-of-the-art devices operate up to 50 GHz, but with ERs less than 10 dB [6,32–34]. We have shown that our device can also operate at 50 GHz, but at the cost of an ER below 10 dB. While the performance is comparable, the modulation efficiencies of the devices reported in the literature are generally between 20 and 50 pm/V, making their energy consumption and device size to be larger than ours. Devices that are also in the low fJ/bit energy consumption range are generally much slower, operating below 20 GHz and 10 dB ER [1,2,24,25]. The improved 2×2 EOM configuration highlights the potential performance of our design, with an ER above 20 dB at the maximum bandwidth; however, a direct comparison is difficult as the prior art is lacking or deficient in this area. By simply comparing our 2×2 to the state-of-the-art 1×1 devices, however, we see comparable or better performance in bandwidth, energy efficiency, ER, and footprint.

Table 2. Comparison to the State-of-the-Art High-Speed EOM, OOL, and OEO Devices

Device	Bandwidth (GHz)	*E/bit* (fJ/bit)	ER (dB)	Radius (μm)	$\Delta\lambda/V$ (pm/V)
OEO (1 × 1)					
This Work	11.1	0.7	17.0	2	250
Previous Work [11]	6.5	5.8	16.6	2	62
OOL (2 × 2)					
This Work	7.6	2.2	12.5	2	250
Previous Work [11]	4.6	9.6	12.3	2	29
EOM					
This Work 1×1	13.4	3.1	10.0	2	250
This Work 1×1	50.3	9.8	3.0	2	170
This Work 2×2	50.3	9.8	24.4	2	170
1×1 [6]	56 (Gb/s)	70	6.0	10	32[a]
1×1 [32]	47	—	6.1	5	45
1×1 [33]	46	710	4.7	—	40
1×1 [34]	80 (Gb/s)	71[b]	—	8	22[a]

[a]Value inferred from transmission spectrum
[b]Value calculated from capacitance and voltage values using $CV^2/4$

6. Conclusion

We present high-efficiency depletion-mode U-junction microdisk modulators for ultrahigh-bandwidth operation in EO modulators, EO logic gates, high-radix EO matrix switches for

Optics EXPRESS

WDM networks, ROADMs, OEO repeaters, OEO wavelength converters, and optical–optical multi-operational logic gates. The U-shaped junction produces a larger change in refractive index and resonance wavelength than conventional, lateral pn junctions, which allows for the use of low-Q, low photon lifetime resonators for high-speed operation of up to 50 GHz under suitably low voltages. The n-p-n sequence of the U-junction becomes fully depleted above the required operating voltage, where the capacitance is reduced below 3 fF. This behaviour allows for a simultaneous high-speed and low-power operation that cannot be demonstrated in conventional, linear single-junction modulators. By using CMOS-compatible materials and processes for the devices presented in this work, we ensure the low-cost, high-volume fabrication feasibility of the proposed designs. Given the impressive performance improvements over the existing devices reported in the literature, our proposed designs offer a promising potential in next-generation electro-optical communications and computing circuits.

Funding

Canada Research Chairs; Natural Sciences and Engineering Research Council of Canada; Air Force Office of Scientific Research (FA9550-17-1-0354, FA9550-19-1-0341).

Disclosures

The authors declare that there are no conflicts of interest related to this article.

References

1. P. Dong, S. Liao, D. Feng, H. Liang, D. Zheng, R. Shafiiha, C.-C. Kung, W. Qian, G. Li, X. Zheng, A. V. Krishnamoorthy, and M. Asghari, "Low Vpp, ultralow-energy, compact, high-speed silicon electro-optic modulator," Opt. Express **17**(25), 22484–22490 (2009).
2. G. Li, X. Zheng, J. Yao, H. Thacker, I. Shubin, Y. Luo, K. Raj, J. E. Cunningham, and A. V. Krishnamoorthy, "25Gb/s 1V-driving CMOS ring modulator with integrated thermal tuning," Opt. Express **19**(21), 20435–20443 (2011).
3. F. Y. Gardes, A. Brimont, P. Sanchis, G. Rasigade, D. Marris-Morini, L. O'Faolain, F. Dong, J. M. Fedeli, P. Dumon, L. Vivien, T. F. Krauss, G. T. Reed, and J. Martí, "High-speed modulation of a compact silicon ring resonator based on a reverse-biased pn diode," Opt. Express **17**(24), 21986–21991 (2009).
4. J.-B. You, M. Park, J.-W. Park, and G. Kim, "12.5 Gbps optical modulation of silicon racetrack resonator based on carrier-depletion in asymmetric pn diode," Opt. Express **16**(22), 18340–18344 (2008).
5. M. Lipson, "Compact electro-optic modulators on a silicon chip," IEEE J. Sel. Top. Quantum Electron. **12**(6), 1520–1526 (2006).
6. J. Sun, R. Kumar, M. Sakib, J. B. Driscoll, H. Jayatilleka, and H. Rong, "A 128 Gb/s PAM4 silicon microring modulator with integrated thermo-optic resonance tuning," J. Lightwave Technol. **37**(1), 110–115 (2019).
7. H. Gevorgyan, A. Khilo, Y. Ehrlichman, and M. A. Popović, "Triply resonant coupled-cavity electro-optic modulators for RF to optical signal conversion," Opt. Express **28**(1), 788–815 (2020).
8. R. Soref, "The past, present, and future of silicon photonics," IEEE J. Sel. Top. Quantum Electron. **12**(6), 1678–1687 (2006).
9. B. Jalali and S. Fathpour, "Silicon photonics," J. Lightwave Technol. **24**(12), 4600–4615 (2006).
10. E. S. Hosseini, S. Yegnanarayanan, A. H. Atabaki, M. Soltani, and A. Adibi, "Systematic design and fabrication of high-Q single-mode pulley-coupled planar silicon nitride microdisk resonators at visible wavelengths," Opt. Express **18**(3), 2127–2136 (2010).
11. R. Soref, F. De Leonardis, Z. Ying, V. M. N. Passaro, and R. T. Chen, "Silicon-based group-IV OEO devices for gain, logic, and wavelength conversion," ACS Photonics **7**(3), 800–811 (2020).
12. D. Gostimirovic and W. N. Ye, "A comparison of microresonator devices for WDM-compatible mode-division multiplexing," Proc. SPIE **11284**, 112841E (2020).
13. Z. Ying, C. Feng, Z. Zhao, R. Soref, D. Pan, and R. T. Chen, "Integrated multi-operand electro-optic logic gates for optical computing," Appl. Phys. Lett. **115**(17), 171104 (2019).
14. Z. Ying, C. Feng, Z. Zhao, S. Dhar, H. Dalir, J. Gu, Y. Cheng, R. Soref, D. Z. Pan, and R. T. Chen, "Electronic-photonic arithmetic logic unit for high-speed computing," Nat. Commun. **11**(1), 2154 (2020).
15. D. Gostimirovic and W. N. Ye, "Ultracompact CMOS-compatible optical logic using carrier depletion in microdisk resonators," Sci. Rep. **7**(1), 12603 (2017).
16. L. Y. Dai, Y. H. Hung, Q. Cheng, and K. Bergman, "Experimental demonstration of PAM-4 transmission through microring silicon photonic Clos switch fabric," in *Optical Fiber Communication Conference (OFC) 2020*, OSA Technical Digest (Optical Society of America, 2020), paper. M1H.3.

Optics EXPRESS

17. Z. Wang, P. Yang, Y. S. Chang, J. Xu, X. Chen, Z. Wang, and J. Feng, "A cross-layer optimization framework for integrated optical switches in data centers," IEEE Trans. Comput.-Aided Des. Integr. Circuits Syst. **39**(3), 640–653 (2020).
18. T. Barwicz, M. A. Popovic, F. Gan, M. S. Dahlem, C. W. Holzwarth, P. T. Rakich, E. P. Ippen, F. X. Kärtner, and H. I. Smith, "Reconfigurable silicon photonic circuits for telecommunication applications," Proc. SPIE **6872**, 68720Z (2008).
19. D. Wu, Y. Wu, Y. Wang, J. An, and X. Hu, "Reconfigurable optical add-drop multiplexer based on thermally tunable micro-ring resonators," Opt. Commun. **367**, 44–49 (2016).
20. N. Parsons, A. Hughes, and R. Jensen, "High radix all-optical switches for software-defined datacenter networks," in *Proceedings of ECOC 2016; 42nd European Conference on Optical Communication*, (VDE, 2016).
21. N. Calabretta, W. Miao, K. Prifti, and K. Williams, "System performance assessment of a monolithically integrated WDM cross-connect switch for optical data centre networks," in *Proceedings of ECOC 2016; 42nd European Conference on Optical Communication*, (VDE, 2016).
22. Z. Wang, J. Xu, P. Yang, Z. Wang, L. H. K. Duong, and X. Chen, "High-radix nonblocking integrated optical switching fabric for data center," J. Lightwave Technol. **35**(19), 4268–4281 (2017).
23. Y. Huang, Q. Cheng, Y. H. Hung, H. Guan, X. Meng, A. Novack, M. Streshinsky, M. Hochberg, and K. Bergman, "Multi-stage 8 (8 silicon photonic switch based on dual-microring switching elements," J. Lightwave Technol. **38**(2), 194–201 (2020).
24. E. Timurdogan, C. M. Sorace-Agaskar, J. Sun, E. S. Hosseini, A. Biberman, and M. R. Watts, "An ultralow power athermal silicon modulator," Nat. Commun. **5**(1), 4008 (2014).
25. M. R. Watts, W. A. Zortman, D. C. Trotter, R. W. Young, and A. L. Lentine, "Vertical junction silicon microdisk modulators and switches," Opt. Express **19**(22), 21989–22003 (2011).
26. Z. Yong, W. D. Sacher, Y. Huang, J. C. Mikkelsen, Y. Yang, X. Luo, X. P. Dumais, D. Goodwill, H. Bahrami, P. Guo-Qiang Lo, E. Bernier, and J. K. S. Poon, "U-shaped PN junctions for efficient silicon Mach-Zehnder and microring modulators in the O-band," Opt. Express **25**(7), 8425–8439 (2017).
27. T. Cao, Y. Fei, L. Zhang, Y. Cao, and S. Chen, "Design of a silicon Mach–Zehnder modulator with a U-type PN junction," Appl. Opt. **52**(24), 5941–5948 (2013).
28. Z. Ying, Z. Wang, Z. Zhao, S. Dhar, D. Z. Pan, R. Soref, and R. T. Chen, "Comparison of microrings and microdisks for high-speed optical modulation in silicon photonics," Appl. Phys. Lett. **112**(11), 111108 (2018).
29. R. Soref and B. Bennett, "Electrooptical effects in silicon," IEEE J. Quantum Electron. **23**(1), 123–129 (1987).
30. Lumerical Inc. https://www.lumerical.com/products/
31. Synopsys Inc. https://www.synopsys.com/silicon/tcad/process-simulation/taurus-tsuprem-4.html
32. M. Pantouvaki, S. A. Srinivasan, Y. Ban, P. De Heyn, P. Verheyen, G. Lepage, H. Chen, J. De Coster, N. Golshani, S. Balakrishnan, P. Absil, and J. Van Campenhout, "Active components for 50 Gb/s NRZ-OOK Optical Interconnects in a solicon photonics platform," J. Lightwave Technol. **35**(4), 631–638 (2017).
33. H. Ramon, M. Vanhoecke, J. Verbist, W. Soenen, P. De Heyn, Y. Ban, M. Pantouvaki, J. Van Campenhout, P. Ossieur, X. Yin, and J. Bauwelinck, "Low-power 56 Gb/s NRZ microring modulator driver in 28 nm FDSOI CMOS," IEEE Photonics Technol. Lett. **30**(5), 467–470 (2018).
34. R. Dubé-Demers, S. LaRochelle, and W. Shi, "Ultrafast pulse-amplitude modulation with a femtojoule silicon photonic modulator," Optica **3**(6), 622–627 (2016).